Reduced Order Model Feedback Control Design: Numerical Implementation in a Thin Shell Model[1]

H.T. Banks, R.C.H. del Rosario and R.C. Smith[2]

Abstract

Reduced order models employing the Lagrange and POD reduced basis methods in numerical approximation and feedback control of systems are presented and numerically tested. The system under consideration is a thin cylindrical shell with surface-mounted piezoceramic actuators. Donnell-Mushtari equations, modified to include Kelvin-Voigt damping, are used to model the system dynamics. Basis functions constructed from Fourier polynomials tensored with cubic splines are employed in the Galerkin expansion of the full order model. Reduced basis elements are then formed from full order approximations of the exogenously excited shell taken at different time instances. Numerical examples illustrating the features of the reduced basis methods are presented. As a first step toward investigating the behavior of the methods when implemented in physical systems, the use of reduced order model feedback control gains in the full order model is considered and numerical examples are presented.

1 Introduction

There is a vast and growing literature on the design of feedback control laws based on partial differential equation (PDE) models for physical systems. Much of the attention has been on theory – for a partial summary see Chapter 7 of [5] and the references cited therein. More recently, efforts to experimentally implement the theoretical ideas from feedback control theory have provided additional stimulus for the development of efficient computational methodologies. In [5, Chapter 8],[4], investigators succeeded in experimentally implementing PDE-based feedback controls and compensators on a simple physical system involving a thin plate, obtaining significant control authority in the context of smart material technologies (in particular, piezoceramic sensing and actuation). The efforts involve real time computationally intensive algorithms which are unlikely to be extended to more complex physical arenas such as shells [7, 8, 9] or structural acoustic systems [2] if the computations are based on usual finite element methods for full-order, physically accurate PDE models. Thus, the success of future efforts in the direction of PDE-based control and compensator design clearly rests in the development of reduced order model based calculations for use in on-line, real-time control methodologies. This note offers a first step in that direction.

We present here some initial computational findings for reduced order model feedback control design using two distinct but related approaches: (i) the so-called reduced basis

[1]Research supported in part by the U.S. Air Force Office of Scientific Research under grants AFSOR F49620-95-1-0236 and AFSOR F49620-98-1-0180

[2]Center for Research in Scientific Computation, Box 8205, NCSU, Raleigh, NC 27695-8205

methods of Lagrange, Taylor and Hermite type and (ii) the (perhaps too) popular proper orthogonal decomposition (POD) methods that are generally attributed to Karhunen and Loève. Our findings, some of which are detailed below and summarized in the concluding section, suggest that in some cases one or the other of these reduced basis method based computational approaches can prove useful in the design of gains which can be implemented in real-time.

The ideas underlying the reduced basis method appear to have their origins in the suggestions of Almroth [1] and Nagy [15] which were developed by Noor and colleagues [16, 17, 18] in the context of simulations for structures and later by Peterson [19] in high Reynolds numbers incompressible viscous flow simulations. The first use of reduced basis methods for open loop control of fluids as described by Navier Stokes type PDE can be found in [10, 11]. Roughly speaking, the reduced basis method employs parameter-dependent solutions of the system to be approximated. These solutions are used to construct basis elements in the hope that solutions at other parameter values can be represented in terms of perturbations of solutions given at carefully chosen parameter values (the Lagrange basis approach) or in terms of a "moving frame" (the Taylor approach). It is important to note that the parameter-dependent solutions used as basis functions can be obtained either from full order model numerical simulations or experimental data.

The POD or Karhunen-Loève methods begin with essentially the same information about the full order system to be approximated. Through an orthogonalization procedure, one then attempts to extract characteristic information from the experimental or numerical solution set and represent this in an "optimal" way in constructing a reduced set of basis elements.

The efforts of Lumley [13], (see also the review in [6]) have stimulated significant research into the use of POD methods in simulations in fluid mechanics (especially turbulence and coherent structures) as well as in image processing and signal analysis (again see [6] and the references therein). The successful use of POD in open loop control problems [14] is very recent.

We discuss here, for the first time to our knowledge, the use of Lagrange and POD reduced basis methods as applied to PDE-based feedback control design. As the reader will see, these methods are not offered as a panacea – they must be used with care and even then may not prove adequate in all regimes. Our goals are to provide a preliminary investigation into what, if any, advantages these approaches can provide to the area of feedback control design for complex physical systems. We chose to do to this in the context of a coupled cylindrical shell model incorporating piezoceramic actuators. This shell paradigm is not an essential feature of our investigations; it does, however, provide a convenient 2-D example for which the full order calculations most likely will, without special efforts, prohibit feedback control design in current on-line computational environments. It is also a model for which we have prior computational experience. The ideas we discuss below should be readily applicable to plates and other structures, structural acoustic systems and more general fluid/structure interaction systems.

In Section 2, we summarize the shell model as developed elsewhere. We discuss briefly general finite dimensional approximations in Section 3 and then present the ideas behind the Lagrange and POD reduced basis methods. The section concludes with uncontrolled shell simulation examples. We begin Section 4 with reduced order model control designs applied to the reduced order model system, which is not what one must do in actual applications. To gain better insight into the performance of the ideas in applications, we finish Section 4 with a discussion on the use of the reduced order designed gains in the full order system.

2 Shell Model

In this section, we present the model for a thin cylindrical shell having piezoceramic patches bonded in pairs to the inner and outer surfaces. As shown in Figure 1, points on the shell have coordinates (x, θ), where the x-axis is aligned with the longitudinal axis of the shell and the θ-axis is oriented along the circumference. The radius of the shell is denoted by R, the thickness by h, the center of the i^{th} patch pair by $(\bar{x}_i, \bar{\theta}_i)$, and the longitudinal, circumferential and tangential displacements of the middle surface by u, v and w, respectively. Furthermore, we denote the density of the shell by ρ, Young's modulus by E_{pe}, Kelvin-Voigt damping parameters by c_D and Poisson ratio by ν. Corresponding parameters for the patches, assumed uniform for all the s pairs, are denoted with the subscript pe and are given by $h_{pe}, \rho_{pe}, E_{pe}$, $c_{D_{pe}}$ and ν_{pe}. Edge coordinates of the i^{th} patch pair are given by $x_{1i}, x_{2i}, \theta_{1i}, \theta_{2i}$. The actuating capabilities of the piezoceramic patches come from material deformations which occur in response to applied voltages, and the proportionality constant d_{31} relates the generated strain to the voltage input. Passive patch contributions in the density, moment and force resultants are neglected and the glue bonding layer is assumed to have negligible contribution to the structural dynamics. For systems incorporating passive patch contributions, see [5, 7], and discussions regarding incorporation of bonding layers in the model could be found in [5].

Shell equations are derived in [5, 12] by considering strain-displacement relations, stress-strain relations, internal force and moment resultants, and equations of motion. By neglecting lower order terms, one obtains the modified Donnell-Mushtari equations

$$
\begin{aligned}
&R\rho h \frac{\partial^2 u}{\partial t^2} - R\frac{\partial N_x}{\partial x} - \frac{\partial N_{\theta x}}{\partial \theta} = R\hat{q}_x - R\sum_{i=1}^{s} \frac{\partial (N_x)_{pe_i}}{\partial x} \mathcal{S}_{pe_i}(x,\theta) \\
&R\rho h \frac{\partial^2 v}{\partial t^2} - \frac{\partial N_\theta}{\partial \theta} - R\frac{N_{x\theta}}{\partial x} = R\hat{q}_\theta - \sum_{i=1}^{s} \frac{\partial (N_\theta)_{pe_i}}{\partial \theta} \mathcal{S}_{pe_i}(x,\theta) \\
&R\rho h \frac{\partial^2 w}{\partial t^2} - R\frac{\partial^2 M_x}{\partial x^2} - \frac{1}{R}\frac{\partial^2 M_\theta}{\partial \theta^2} - 2\frac{\partial^2 M_{x\theta}}{\partial x \partial \theta} + N_\theta \\
&\qquad\qquad = R\hat{q}_n - \sum_{i=1}^{s}\left[R\frac{\partial^2 (M_x)_{pe_i}}{\partial x^2} + \frac{1}{R}\frac{\partial^2 (M_\theta)_{pe_i}}{\partial \theta^2}\right].
\end{aligned} \tag{1}
$$

External surface forces in the longitudinal, circumferential and transverse directions are modeled by the functions $\hat{q}_x, \hat{q}_\theta$ and $\hat{q}_n$ respectively. As detailed in [5], the internal force and moment resultants $N_x, N_\theta, N_{x\theta}, N_{\theta x}, M_x, M_\theta, M_{x\theta}$ have the form

$$
\begin{aligned}
N_x &= \frac{Eh}{(1-\nu^2)}\left[\frac{\partial u}{\partial x}+\nu\left(\frac{1}{R}\frac{\partial v}{\partial \theta}+\frac{w}{R}\right)\right]+\frac{c_D h}{(1-\nu^2)}\frac{\partial}{\partial t}\left[\frac{\partial u}{\partial x}+\nu\left(\frac{1}{R}\frac{\partial v}{\partial \theta}+\frac{w}{R}\right)\right]\\
N_\theta &= \frac{Eh}{(1-\nu^2)}\left[\frac{1}{R}\frac{\partial v}{\partial \theta}+\frac{w}{R}+\nu\frac{\partial u}{\partial x}\right]+\frac{c_D h}{(1-\nu^2)}\frac{\partial}{\partial t}\left[\frac{1}{R}\frac{\partial v}{\partial \theta}+\frac{w}{R}+\nu\frac{\partial u}{\partial x}\right]\\
N_{x\theta} = N_{\theta x} &= \frac{Eh}{2(1+\nu)}\left[\frac{\partial v}{\partial x}+\frac{1}{R}\frac{\partial u}{\partial \theta}\right]+\frac{c_D h}{2(1+\nu)}\frac{\partial}{\partial t}\left[\frac{\partial v}{\partial x}+\frac{1}{R}\frac{\partial u}{\partial \theta}\right]\\
M_x &= -\frac{Eh^3}{12(1-\nu^2)}\left[\frac{\partial^2 w}{\partial x^2}+\frac{\nu}{R^2}\frac{\partial^2 w}{\partial \theta^2}\right]-\frac{c_D h^3}{12(1-\nu^2)}\frac{\partial}{\partial t}\left[\frac{\partial^2 w}{\partial x^2}+\frac{\nu}{R^2}\frac{\partial^2 w}{\partial \theta^2}\right]\\
M_\theta &= -\frac{Eh^3}{12(1-\nu^2)}\left[\frac{1}{R^2}\frac{\partial^2 w}{\partial \theta^2}+\nu\frac{\partial^2 w}{\partial x^2}\right]-\frac{c_D h^3}{12(1-\nu^2)}\frac{\partial}{\partial t}\left[\frac{1}{R^2}\frac{\partial^2 w}{\partial \theta^2}+\nu\frac{\partial^2 w}{\partial x^2}\right]\\
M_{x\theta} = M_{\theta x} &= -\frac{Eh^3}{12R(1+\nu)}\frac{\partial^2 w}{\partial x\partial\theta}-\frac{c_D h^3}{12R(1+\nu)}\frac{\partial}{\partial t}\left[\frac{\partial^2 w}{\partial x\partial\theta}\right].
\end{aligned}
\tag{2}
$$

The patch-induced external resultants $(N_x)_{pe_i}$ and $(N_\theta)_{pe_i}$ produce forces which are opposite in direction at points symmetric to the center $(\bar{x}_i, \bar{\theta}_i)$ of the i^{th} patch. This is modeled by the the indicator function $\mathcal{S}_{pe_i}(x,\theta) = S_{1,2}(x)\hat{S}_{1,2}(\theta)$, where

$$
S_{1,2}(x) = \begin{cases} 1 & , \quad x < (x_{1i}+x_{2i})/2 \\ 0 & , \quad x = (x_{1i}+x_{2i})/2 \\ -1 & , \quad x > (x_{1i}+x_{2i})/2 \end{cases} , \quad \hat{S}_{1,2}(\theta) = \begin{cases} 1 & , \quad \theta < (\theta_{1i}+\theta_{2i})/2 \\ 0 & , \quad \theta = (\theta_{1i}+\theta_{2i})/2 \\ -1 & , \quad \theta > (\theta_{1i}+\theta_{2i})/2 \end{cases} .
$$

Denoting the outer and inner input voltages by $V_{1i}(t)$ and $V_{2i}(t)$, respectively, the external force and moment resultants, as derived in [5], are given by

$$
\begin{aligned}
(M_x)_{pe_i} &= \frac{-E_{pe}d_{31}}{(1-\nu_{pe})h_{pe}}\left[\left(\frac{a_2}{2}+\frac{a_3}{3R}\right)V_{1i}-\left(\frac{a_2}{2}-\frac{a_3}{3R}\right)V_{2i}\right]\chi_{pe_i}(x,\theta)\\
(M_\theta)_{pe_i} &= \frac{-E_{pe}d_{31}a_2}{2(1-\nu_{pe})h_{pe}}\left[V_{1i}-V_{2i}\right]\chi_{pe_i}(x,\theta)\\
(N_x)_{pe_i} &= \frac{-E_{pe}d_{31}}{(1-\nu_{pe})h_{pe}}\left[\left(h_{pe}+\frac{a_2}{2R}\right)V_{1i}+\left(h_{pe}-\frac{a_2}{2R}\right)V_{2i}\right]\chi_{pe_i}(x,\theta)\mathcal{S}_{pe_i}(x,\theta)\\
(N_\theta)_{pe_i} &= \frac{-E_{pe}}{1-\nu_{pe}}d_{31}[V_{1i}-V_{2i}]\chi_{pe_i}(x,\theta)\mathcal{S}_{pe_i}(x,\theta)
\end{aligned}
\tag{3}
$$

where the constants $a_2 = (h/2+h_{pe})^2 - h^2/4$ and $a_3 = (h/2+h_{pe})^3 - h^3/8$ arise from integrating through the thickness of the patch. The characteristic function $\chi_{pe_i}(x,\theta)$ with value 1 in the region covered by the i^{th} patch and zero elsewhere indicates the patch contributions to regions of the shell covered by the patches.

To accommodate commonly employed experimental edge clamps, we consider clamped edge boundary conditions expressed as

$$u(t,0,\theta)=u(t,\ell,\theta)=v(t,0,\theta)=v(t,\ell,\theta) \quad = \quad 0 \tag{4a}$$

$$w(t,0,\theta)=w(t,\ell,\theta)=\frac{\partial w(t,0,\theta)}{\partial x}=\frac{\partial w(t,\ell,\theta)}{\partial x} \quad = \quad 0\;. \tag{4b}$$

For approximation and theoretical analysis (see [8, 9]) we consider the weak form of the equations

$$\begin{aligned}
\int_{\Gamma_0}\left\{R\rho h\frac{\partial^2 u}{\partial t^2}\eta_1+RN_x\frac{\partial\eta_1}{\partial x}+N_{\theta x}\frac{\partial\eta_1}{\partial\theta}-R\hat{q}_x\eta_1-R\sum_{i=1}^{s}(N_x)_{pe_i}\frac{\partial\eta_1}{\partial x}\right\}d\gamma &= 0\\
\int_{\Gamma_0}\left\{R\rho h\frac{\partial^2 v}{\partial t^2}\eta_2+N_\theta\frac{\partial\eta_2}{\partial\theta}+RN_{x\theta}\frac{\partial\eta_2}{\partial x}-R\hat{q}_\theta\eta_2-\sum_{i=1}^{s}(N_\theta)_{pe_i}\frac{\partial\eta_2}{\partial\theta}\right\}d\gamma &= 0\\
\int_{\Gamma_0}\left\{R\rho h\frac{\partial^2 w}{\partial t^2}\eta_3+N_\theta\eta_3-RM_x\frac{\partial^2\eta_3}{\partial x^2}-\frac{1}{R}M_\theta\frac{\partial^2\eta_3}{\partial\theta^2}-2M_{x\theta}\frac{\partial^2\eta_3}{\partial x\partial\theta}\right.&\\
\left.-R\hat{q}_n\eta_3+\sum_{i=1}^{s}\left[R(M_x)_{pe_i}\frac{\partial^2\eta_3}{\partial x^2}+\frac{1}{R}(M_\theta)_{pe_i}\frac{\partial^2\eta_3}{\partial\theta^2}\right]\right\}d\gamma &= 0
\end{aligned} \tag{5}$$

for all test functions $\Psi=(\eta_1,\eta_2,\eta_3)$ (see [5] for details). Here Γ_0 denotes the region occupied by the middle surface of the shell, i.e., $\Gamma_0=\{(x,\theta):0\le x\le\ell, 0\le\theta\le 2\pi\}$. The state variables for the system are taken to be $y=(u,v,w)$ in the state space

$$H=L^2(\Gamma_0)\times L^2(\Gamma_0)\times L^2(\Gamma_0)\;.$$

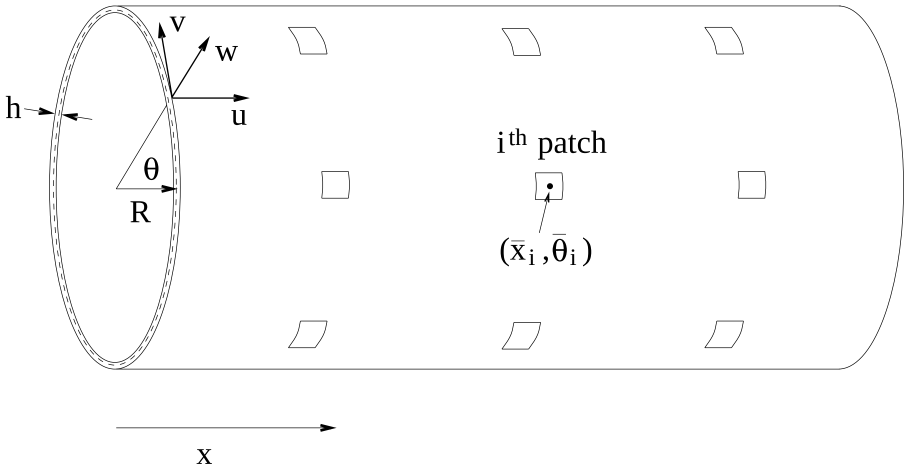

Figure 1. Thin cylindrical shell with surface mounted piezoceramic patches.

To satisfy boundary conditions and smoothness criteria, we take the space of test functions to be

$$V = H_0^1(\Gamma_0) \times H_0^1(\Gamma_0) \times H_0^2(\Gamma_0) \ , \tag{6}$$

where

$$H_0^1(\Gamma_0) = \left\{ \eta \in H^1(\Gamma_0) : \eta(0,\cdot) = \eta(\ell,\cdot) = 0 \right\}$$
$$H_0^2(\Gamma_0) = \left\{ \eta \in H^2(\Gamma_0) : \eta(0,\cdot) = \frac{\partial \eta(0,\cdot)}{\partial x} = \eta(\ell,\cdot) = \frac{\partial \eta(\ell,\cdot)}{\partial x} = 0 \right\}.$$

Note that $V \subset H$.

3 Approximation Methods

In this section, we describe the Galerkin methods employed to numerically approximate the system (5). The convergence, accuracy and efficiency of the methods depend heavily on the type of basis elements used in creating the finite dimensional system. Standard basis functions such as cubic or linear splines result in large dimensional systems requiring intensive computations and thus are not suitable for real-time implementation. We investigate two reduced basis methods, the Lagrange and proper orthogonal decomposition methods, which give a 97% reduction in the dimension of the finite dimensional system. Numerical results illustrating the features of the two methods are presented at the end of the section.

The general approximation strategy can be summarized as follows. We approximate the solution $y = (u, v, w)$ by restricting the state space to a finite dimensional subset $V^{\mathcal{N}} \subset V \subset H$. The $\mathcal{N}$-dimensional subspace $V^{\mathcal{N}}$ is then formed by choosing basis functions $\{\mathcal{B}_{u_i}\}_{i=1}^{\mathcal{N}_u}$, $\{\mathcal{B}_{v_i}\}_{i=1}^{\mathcal{N}_v}$ and $\{\mathcal{B}_{w_i}\}_{i=1}^{\mathcal{N}_w}$ and setting

$$V^{\mathcal{N}} = \mathrm{span}\{\mathcal{B}_{u_i}\}_{i=1}^{\mathcal{N}_u} \times \mathrm{span}\{\mathcal{B}_{v_i}\}_{i=1}^{\mathcal{N}_v} \times \mathrm{span}\{\mathcal{B}_{w_i}\}_{i=1}^{\mathcal{N}_w} \ , \tag{7}$$

where $\mathcal{N} = \mathcal{N}_u + \mathcal{N}_v + \mathcal{N}_w$. Finally, we form the Galerkin expansions

$$y^{\mathcal{N}}(t,x,\theta) = \begin{bmatrix} u^{\mathcal{N}}(t,x,\theta) \\ v^{\mathcal{N}}(t,x,\theta) \\ w^{\mathcal{N}}(t,x,\theta) \end{bmatrix} = \begin{bmatrix} \sum_{i=1}^{\mathcal{N}_u} u_i(t)\mathcal{B}_{u_i}(x,\theta) \\ \sum_{i=1}^{\mathcal{N}_v} v_i(t)\mathcal{B}_{v_i}(x,\theta) \\ \sum_{i=1}^{\mathcal{N}_w} w_i(t)\mathcal{B}_{w_i}(x,\theta) \end{bmatrix} \ , \tag{8}$$

and the approximating system is determined by restricting the weak form (5) to $V^{\mathcal{N}}$ with basis functions used as test functions. This is equivalent to orthogonalizing the residual with respect to elements from $V^{\mathcal{N}}$. To write the approximating system in first-order form, we consolidate the generalized coefficients $u_i(t), v_i(t)$ and $w_i(t)$ into one vector

$$\vartheta^{\mathcal{N}}(t) = [u_1(t), \ldots, u_{\mathcal{N}_u}(t), v_1(t), \ldots, v_{\mathcal{N}_v}(t), w_1(t), \ldots, w_{\mathcal{N}_w}(t)]^T \in \mathbb{R}^{\mathcal{N}} \ ,$$

and the resulting matrix system becomes

$$\begin{aligned}
&\begin{bmatrix} K_E^{\mathcal{N}} & 0 \\ 0 & M^{\mathcal{N}} \end{bmatrix} \begin{bmatrix} \dot{\vartheta}^{\mathcal{N}}(t) \\ \ddot{\vartheta}^{\mathcal{N}}(t) \end{bmatrix} = \begin{bmatrix} 0 & K_E^{\mathcal{N}} \\ -K_E^{\mathcal{N}} & -K_{C_D}^{\mathcal{N}} \end{bmatrix} \begin{bmatrix} \vartheta^{\mathcal{N}}(t) \\ \dot{\vartheta}^{\mathcal{N}}(t) \end{bmatrix} + \begin{bmatrix} 0 \\ \hat{B}^{\mathcal{N}} \end{bmatrix} U(t) + \begin{bmatrix} 0 \\ \hat{F}^{\mathcal{N}}(t) \end{bmatrix} \\
&\begin{bmatrix} K_E^{\mathcal{N}} & 0 \\ 0 & M^{\mathcal{N}} \end{bmatrix} \begin{bmatrix} \vartheta^{\mathcal{N}}(0) \\ \dot{\vartheta}^{\mathcal{N}}(0) \end{bmatrix} = \begin{bmatrix} y_1^{\mathcal{N}} \\ y_2^{\mathcal{N}} \end{bmatrix} .
\end{aligned} \tag{9}$$

Here the control input vector $U(t)$ has elements

$$U(t) = [V_{11}(t), V_{21}(t), \ldots, V_{s1}(t), V_{s2}(t)]^T \in \mathbb{R}^{2s} ,$$

where s is the number of patch pairs. The reader is referred to Section 4.4 of [7] for details concerning the creation of the matrices $K_E^{\mathcal{N}}, M^{\mathcal{N}}, K_{C_D}^{\mathcal{N}}, \hat{B}^{\mathcal{N}}$ and force vector $\hat{F}^{\mathcal{N}}$. To write the system in a form suitable for simulations, parameter estimation and control applications, we invert the first-order system mass matrix to yield a first-order Cauchy equation of the form

$$\begin{aligned}
\dot{z}^{2\mathcal{N}}(t) &= A^{2\mathcal{N}} z^{2\mathcal{N}}(t) + B^{2\mathcal{N}} U(t) + G^{2\mathcal{N}}(t) \\
z^{2\mathcal{N}}(0) &= z_0^{2\mathcal{N}} ,
\end{aligned} \tag{10}$$

where $z^{2\mathcal{N}}(t) = [\vartheta^{\mathcal{N}}(t), \dot{\vartheta}^{\mathcal{N}}(t)] \in \mathbb{R}^{2\mathcal{N}}$. Three approximation methods, identified by the basis functions used, are summarized below.

3.1 Full Order Basis Methods

Use of standard Galerkin basis elements such as cubic splines, linear splines or Legendre polynomials will be referred to as *full order basis methods*. Full order methods employing cubic splines in the x-direction and Fourier polynomials in the circumferential direction were investigated in [7], [8] and [9]. The choice of these basis elements was motivated by smoothness, convergence and accuracy criteria. It was shown that a large dimension of $\mathcal{N} = 333$ basis elements, resulting in a first-order system (10) of dimension $2\mathcal{N} = 666$, was needed to fully approximate the shell equations. The reduced basis methods we discuss below involve the use of a much smaller (e.g., $\mathcal{N} = 9$) approximating subspace of $V^{\mathcal{N}}$ in order to reduce the dimension of the systems (9) and (10).

3.2 Lagrange Reduced Basis Method

The basis elements in the Lagrange subspace are snapshots of the model obtained by solving the system (5) using a full order method. Thus, the basis elements in the u, v and w directions are taken to be $\{\mathcal{B}_{u_i}(x,\theta)\}_{i=1}^{\mathcal{N}_u} = \{u^{\mathcal{N}}(t_i,x,\theta)\}_{i=1}^{\mathcal{N}_u}$, $\{\mathcal{B}_{v_i}(x,\theta)\}_{i=1}^{\mathcal{N}_v} = \{v^{\mathcal{N}}(t_i,x,\theta)\}_{i=1}^{\mathcal{N}_v}$ and $\{\mathcal{B}_{w_i}(x,\theta)\}_{i=1}^{\mathcal{N}_w} = \{w^{\mathcal{N}}(t_i,x,\theta)\}_{i=1}^{\mathcal{N}_w}$, respectively. If experimental data is available, actual measurements of the displacements can also be used as reduced basis elements. Alternatives to the Lagrange reduced basis method, as discussed in [10, 11], include (i) the Hermite reduced basis method where basis elements are full order solutions and their first (time) derivatives, and (ii) the Taylor reduced basis method where basis elements are taken to be a solution at one time instance together with its $\mathcal{N} - 1$ time derivatives.

3.3 Proper Orthogonal Decomposition (POD) Reduced Basis Method

Given N_s snapshots of the model $\{y^{\mathcal{N}}(t_j,x,\theta)\} = \{(u^{\mathcal{N}}(t_j,x,\theta), v^{\mathcal{N}}(t_j,x,\theta), w^{\mathcal{N}}(t_j,x,\theta))\}$ at time instances $t_j, j = 1,\ldots,N_s$, we seek basis elements of the form

$$\begin{aligned}
\mathcal{B}_{u_i}(x,\theta) &= \sum_{j=1}^{N_s} \bar{\alpha}_j^i u^{\mathcal{N}}(t_j,x,\theta) \\
\mathcal{B}_{v_i}(x,\theta) &= \sum_{j=1}^{N_s} \bar{\beta}_j^i v^{\mathcal{N}}(t_j,x,\theta) \\
\mathcal{B}_{w_i}(x,\theta) &= \sum_{j=1}^{N_s} \bar{\gamma}_j^i w^{\mathcal{N}}(t_j,x,\theta)\ .
\end{aligned} \tag{11}$$

As described in [6, 14], the vector of coefficients $\bar{\alpha}^i, \bar{\beta}^i, \bar{\gamma}^i \in \mathbb{R}^{N_s}$ are taken to be the i^{th} eigenvectors of the covariant matrices C_u, C_v, C_w, respectively, with the matrix C_u defined by

$$[C_u]_{k\ell} = \frac{1}{N_s}\left\langle u^{\mathcal{N}}(t_k,x,\theta), u^{\mathcal{N}}(t_\ell,x,\theta)\right\rangle\ , \quad k,\ell = 1,\ldots,N_s\ . \tag{12}$$

The matrices C_v and C_w are defined similarly. Since the matrix C_u is nonnegative and Hermitian, it has a complete set of orthogonal eigenvectors with corresponding eigenvalues $\lambda_1 \geq \lambda_2 \geq \ldots \geq \lambda_{N_s} \geq 0$. We choose the eigenvectors $\bar{\alpha}^i$ such that

$$\bar{\alpha}^k \cdot \bar{\alpha}^\ell = \begin{cases} 0\ , & k \neq \ell \\ \dfrac{1}{N_s\lambda_k}\ , & k = \ell\ . \end{cases}$$

The eigenvectors $\bar{\beta}^i$ and $\bar{\gamma}^i$ of C_v and C_w are chosen similarly.

The basis elements $\mathcal{B}_{u_i}$ are shown to be orthonormal in [14]. Furthermore, the lemma given below from [14] establishes the optimality of the basis, for example $\{\mathcal{B}_{u_i}\}$, in the sense that the approximation $u^{\mathcal{N}}$ using the POD basis to the solution $u \in L^2(0,T;L^2(\Gamma_0))$ contains the most "displacement energy" possible in a time average sense. (For a full discussion of this measure of optimality of the POD method, see for example, [6]).

Lemma 1 *Let $\{\Phi_1,\Phi_2,\ldots,\Phi_{N_s}\}$ denote the orthonormal set of POD basis elements and $\lambda_1 \geq \ldots \geq \lambda_{N_s}$ denote the corresponding set of eigenvalues. If $y^N = \sum_{i=1}^{N_s} b_i(t)\Phi_i$ denotes the approximation to y with respect to this basis, then for any arbitrary orthonormal basis $\{\psi_1,\psi_2,\ldots,\psi_{N_s}\}$ the following hold*

1. $\ll b_i(t)b_j^*(t) \gg\ =\ \delta_{ij}\lambda_i$, *where* $\ll\cdot\gg$ *denotes the average over time,*

2. *for every* N_s, $\displaystyle\sum_{i=1}^{N_s} \ll b_i(t)b_j^*(t) \gg = \sum_{i=1}^{N_s}\lambda_i \geq \sum_{i=1}^{N_s} \ll a_i(t)a_j^*(t) \gg\ ,$

where the $a_i(t)$ are coefficients of the approximation to y, $y^N = \sum_{i=1}^{N_s} a_i(t)\psi_i$, using the arbitrary basis $\{\psi_j\}_{j=1}^{N_s}$.

To determine the dimension of the reduced basis space in the u direction, we determine the integer $\mathcal{N}_u$ such that the sum of the first $\mathcal{N}_u$ eigenvalues gives a good approximation to the sum of all the eigenvalues, i.e., $\sum_{i=1}^{\mathcal{N}_u} \lambda_i \simeq \sum_{i=1}^{N_s} \lambda_i$. The ratio $\sum_{i=1}^{\mathcal{N}_u} \lambda_i \Big/ \sum_{i=1}^{N_s} \lambda_i$ gives the percentage "energy" of the full order model contained in the POD reduced order model. The dimensions $\mathcal{N}_v$ and $\mathcal{N}_w$ are determined by considering the eigenvalue ratios of the matrices C_v and C_w, respectively.

3.4 Numerical Example

The following numerical example illustrates the use of Lagrange and POD reduced order methods and compares their performance with full order methods. The shell and patch parameters used are given in Table 1 below. External excitation is modeled by a periodic noise source localized near the axial shell center ($x = \ell/2$) and at $\theta = 0$ and $\theta = \pi$ with definition

$$\begin{aligned} \hat{q}_x(x,\theta,t) &= \frac{1}{100} e^{-20(x-\ell/2)^2} \Theta(\theta) g(t) \\ \hat{q}_\theta(x,\theta,t) &= 0 \\ \hat{q}_\eta(x,\theta,t) &= e^{-20(x-\ell/2)^2} \Theta(\theta) g(t) \end{aligned} \quad , \; \Theta(\theta) = \begin{cases} 1 - e^{-(\theta-\pi/2)^6/2} & , \quad 0 \le \theta < \pi \\ 1 - e^{-(\theta-3\pi/2)^6/2} & , \quad \pi \le \theta < 2\pi \end{cases} , \tag{13}$$

and

$$g(t) = \sin(640\pi t) + \sin(880\pi t) + \sin(1200\pi t) + \sin(1320\pi t) + \sin(1640\pi t) \; . \tag{14}$$

Note that the temporal component $g(t)$ contains five frequencies. Time history plots are created by recording displacements at the point p_1 on the shell with coordinates $p_1 = (\hat{x}, \hat{\theta}) = (3\ell/4, \pi/4)$. In the succeeding sections, control attenuation is illustrated by plotting root mean square (RMS) displacements along the lines L_1 and L_2 on the shell. In Figure 2, we depict the location of the point p_1, the spatial distribution of the external forcing function (13), and location of the lines $L_1 = \{(x,\theta) | 0 \le x \le \ell, \theta = \pi/6\}$ and $L_2 = \{(x,\theta) | x = 3\ell/4, 0 \le \theta \le 2\pi\}$.

Full order simulations, used as a baseline for comparison with reduced order methods, were obtained using discretization levels of $\mathcal{N}_u = \mathcal{N}_v = 117$ and $\mathcal{N}_w = 99$, for a total of $\mathcal{N} = 333$ basis elements in the second order system and $2\mathcal{N} = 666$ in the first-order system. The additional zero-slope boundary condition (4b) had to be satisfied by the cubic spline/Fourier polynomial basis elements in the w direction and hence $\mathcal{N}_w$ is less than $\mathcal{N}_u$ and $\mathcal{N}_v$ (see [3] for a more detailed discussion).

Reduced basis method approximations are compared with full order solutions using the ℓ_1 norm of the difference between the displacements. This is done by taking 500 full and reduced order point displacements at p_1 over the time interval simulation, and summing the absolute value of the difference between the reduced order and full order dispacements.

Lagrange Reduced Order Method:

The Lagrange reduced order method was tested using discretization sizes of $\mathcal{N}_u = \mathcal{N}_v = \mathcal{N}_w = 1, 2, 3$ and 4 ($\mathcal{N} = 3, 6, 9$ and 12). Note that as opposed to the full order method, the same discretization levels could be used for each displacement direction because each reduced basis function (being a full order solution) already satisfies the boundary conditions. We also point out that uniform discretization in the three directions were used for ease in exposition and that the user could choose to do otherwise. For each discretization level, intuition was used to obtain the time instances at which reduced basis functions will be realized to obtain the best approximation. Over the time interval $t = [0, 0.1]s$, our experience revealed that the least ℓ_1 errors are obtained with basis functions taken at the time following time instances: (i) $\mathcal{N} = 3, t_i = 0.0333s$; (ii) $\mathcal{N} = 6, t_i = \{0.0200, 0.0667s\}$; (iii) $\mathcal{N} = 9, t_i = \{0.0200, 0.0333, 0.0667s\}$; (iv) $\mathcal{N} = 12, t_i = \{0.0200, 0.0500, 0.0.0667, 0.1\}$. It is seen in Table 2, where we present the ℓ_1 norm of the difference between full and reduced order approximations, that the ℓ_1 error decreases as the dimension of the Lagrange basis increases. One shortcoming of this method is the tendency of the condition numbers to become very large as the number of basis functions increases. To illustrate this, the condition number κ of the mass matrix $M^{\mathcal{N}}$ and stiffness matrix $K_E^{\mathcal{N}}$ are also reported in Table 2.

The time histories at the point p_1 using $\mathcal{N} = 9$ Lagrange basis functions together with trajectories from the full order and POD model (whose implementation will be discussed shortly) are presented in Figure 3 below. It could be seen from the plots that the full order, Lagrange and POD approximations are graphically indistinguishable from each other and that the reduced order models give a good approximation to the full order system. Since numerical results with $\mathcal{N} = 6$ and 12 Lagrange basis functions are similar to those with 9 basis functions, the plots are not given here. As shown by the large ℓ_1 error in Table 2, the system is not fully approximated with $\mathcal{N} = 3$ basis functions so the displacements are not reported (see [3, p. 10] for illustrations).

<table>
<tr><th></th><th>Dimensions</th><th>Parameters</th></tr>
<tr><td>Shell</td><td>$h = .00127m$
$R = .4m$
$\ell = 1m$</td><td>$\rho = 2700kg/m^3$
$E = 7.1 \times 10^{10} N/m^2$
$c_D = 1.47 \times 10^5 Nms$
$\nu = .33$</td></tr>
<tr><td>Patches</td><td>$h_{pe} = .0001778m$
Centers (x, θ): (.25,0), (.5,0), (.75,0)
$(.25, \pi/2)$, $(.5, \pi/2)$, $(.75, \pi/2)$
$(.25, \pi)$, $(.5, \pi)$, $(.75, \pi)$
$(.25, 3\pi/2)$, $(.5, 3\pi/2)$, $(.75, 3\pi/2)$</td><td>$\rho_{pe} = 7600kg/m^3$
$E_{pe} = 6.3 \times 10^{10} N/m^2$
$c_{D_{pe}} = 1.7 \times 10^5 Nms$
$\nu_{pe} = .31$
$d_{31} = 190 \times 10^{-12} m/V$</td></tr>
</table>

Table 1. Dimensions and physical parameters for the shell and patches.

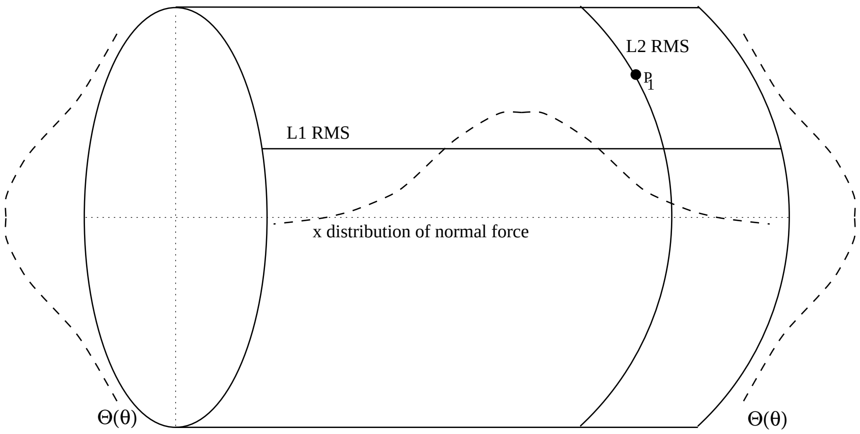

Figure 2. Location of the point p_1, RMS line $L_1 = \{(x,\theta)|0 \le x \le \ell, \theta = \pi/6\}$, RMS line $L_2 = \{(x,\theta)|x = 3\ell/4, 0 \le \theta \le 2\pi\}$ and spatial distribution of the exogenous force.

$\mathcal{N}$	$\|udiff\|_{\ell_1}$	$\|vdiff\|_{\ell_1}$	$\|wdiff\|_{\ell_1}$	$\kappa(M^{\mathcal{N}})$	$\kappa(K_E^{\mathcal{N}})$
3	3.23e-05	2.33e-04	6.20e-04	1.4e+00	2.0e+02
6	1.61e-06	1.74e-06	2.55e-05	3.2e+00	1.3e+03
9	5.37e-07	3.83e-07	9.61e-06	8.3e+04	1.8e+05
12	5.32e-08	2.63e-07	3.25e-07	9.7e+05	3.8e+07

Table 2. ℓ_1 norm of the difference between full and Lagrange reduced order models and condition numbers of the mass $(M^{\mathcal{N}})$ and stiffness $(K_E^{\mathcal{N}})$ matrices.

POD Reduced Order Method:

The POD reduced order method was tested by obtaining $\mathcal{N}_s = 20$ snapshots of the model from which POD basis functions of the form (11) are created. As in the Lagrange simulations, $\mathcal{N} = 3, 6, 9$ and 12 discretization levels were employed. In Table 3 we note that the ℓ_1 norm of the difference between solutions of the full order and POD reduced order models decreases as the dimension of the reduced basis space increases. Moreover, condition numbers of the mass and stiffness matrices remain small as more basis functions are added. The condition number 1 for all mass matrices $M^{\mathcal{N}}$ in Table 3 results from the orthogonality of POD basis functions. We point out that even though the ℓ_1 error of the difference between the full order and Lagrange reduced order method approximations are slightly better as reported in Table 2, the basis functions there were chosen, using intuition and trial and error, to give good approximations, and so that level of accuracy is generally much more difficult for users to attain. As mentioned earlier, displacements at the point p_1 using $\mathcal{N} = 9$ POD basis functions, together with full order and Lagrange reduced order approximations are illustrated in Figure 3. As in the Lagrange method, results with $\mathcal{N} = 6$ and 12 are similar to those with $\mathcal{N} = 9$ and hence are not reported. Only 52%, 59% and 54% of the full order model energy in the u, v and w directions, respectively, were captured by the POD method with $\mathcal{N} = 3$ basis functions, indicating poor approximation at this discretization level. Hence plots with $\mathcal{N} = 3$ are not given here. The energy percentage increased to 99.9% (for each of the three directions) when $\mathcal{N} = 6$ basis functions were employed and thus, as expected, discretization levels of at least $\mathcal{N} = 6$ provided good approximation to the full order system (see Table 3).

$\mathcal{N}$	$\|udiff\|_{\ell_1}$	$\|vdiff\|_{\ell_1}$	$\|wdiff\|_{\ell_1}$	$\kappa(M^{\mathcal{N}})$	$\kappa(K_E^{\mathcal{N}})$
3	3.28e-05	2.36e-04	6.31e-04	1.0e+00	1.2e+01
6	1.71e-06	3.66e-06	2.62e-05	1.0e+00	1.0e+03
9	4.03e-07	2.97e-07	7.22e-06	1.0e+00	1.1e+03
12	2.70e-07	2.48e-07	4.84e-06	1.0e+00	1.9e+03

Table 3. ℓ_1 norm of the difference between full and POD reduced order models and condition numbers of the mass ($M^{\mathcal{N}}$) and stiffness ($K_E^{\mathcal{N}}$) matrices.

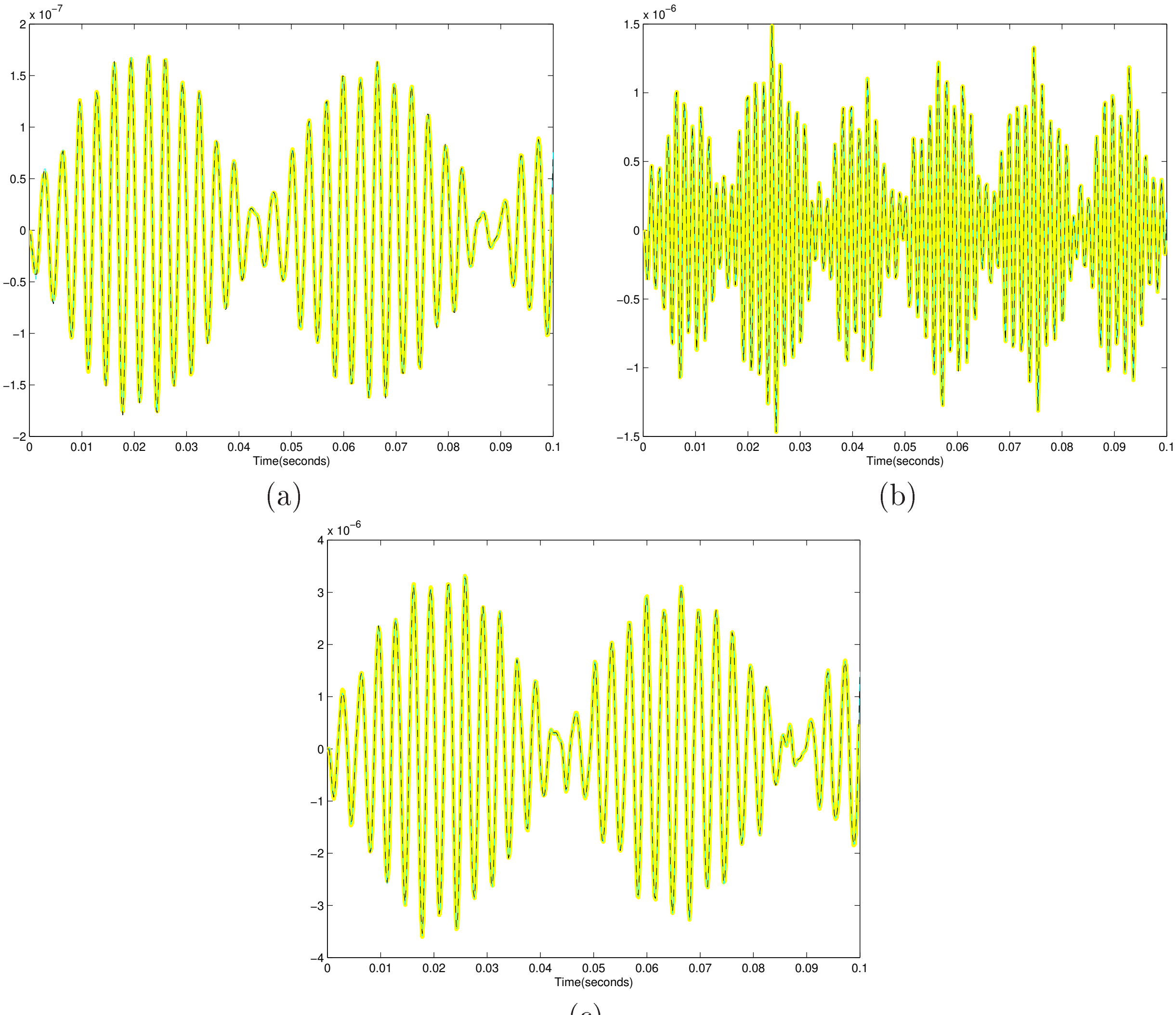

Figure 3. Point displacements at $p_1 = (\hat{x}, \hat{\theta}) = (3\ell/4, \pi/4)$; (a) longitudinal $u^{\mathcal{N}}(t, \hat{x}, \hat{\theta})$, (b) circumferential $v^{\mathcal{N}}(t, \hat{x}, \hat{\theta})$, (c) transverse $w^{\mathcal{N}}(t, \hat{x}, \hat{\theta})$; —— full order ($\mathcal{N} = 333$), —— Lagrange ($\mathcal{N} = 9$), - - POD ($\mathcal{N} = 9$). The graphs are indistinguishable from each other due to the small difference between full order and reduced basis trajectories.

4 Control Problem

In this section, we briefly discuss a feedback control methodology for the shell system (10) excited by a periodic exogenous force given by (13) and (14). Numerical examples illustrating methods based upon the full order, Lagrange and POD reduced order models are presented. In the second half of the section, we develop a method to implement reduced order based controls in the full order model and present numerical results.

As detailed in [5, 8, 9], feedback gains based on Riccati operators $\Pi^{2\mathcal{N}}$ and optimal controls $U(t)$ are determined by minimizing the standard quadratic functional

$$J(U, z_0^{2\mathcal{N}}) = \frac{1}{2}\int_0^\tau \left\{ \left\langle Q^{2\mathcal{N}} z^{2\mathcal{N}}(t), z^{2\mathcal{N}}(t) \right\rangle + \left\langle R^{2s} U(t), U(t) \right\rangle \right\} dt \tag{15}$$

subject to the system

$$\begin{aligned} \dot{z}^{2\mathcal{N}}(t) &= A^{2\mathcal{N}} z^{2\mathcal{N}}(t) + B^{2\mathcal{N}} U(t) + G^{2\mathcal{N}}(t) \\ z^{2\mathcal{N}}(0) &= z_0^{2\mathcal{N}} \ , \end{aligned} \tag{16}$$

where τ is the period of the exogenous force $G^{2\mathcal{N}}$ and $U(t) \in \mathbb{R}^{2s}$ (s is the number of patch pairs). We point out that (16) can be obtained using the full order, Lagrange, or POD approximation methods with the dimension $\mathcal{N}$ dictated by the order of the method. The displacements and voltages to the patches are weighted using the matrices $Q^{2\mathcal{N}}$ and R^{2s}, respectively. As detailed in Chapters 8 and 9 of [5], the optimal control which minimizes (15) is given in feedback form by

$$\overline{U}(t) = -R^{2s}\left(B^{2\mathcal{N}}\right)^T \left[\Pi^{2\mathcal{N}} \bar{z}^{2\mathcal{N}}(t) - r^{2\mathcal{N}}(t)\right] \ , \tag{17}$$

where the τ-periodic trajectory $\bar{z}^{2\mathcal{N}}(t)$ is obtained by solving the closed loop system

$$\begin{aligned} \dot{z}^{2\mathcal{N}}(t) &= \left[A^{2\mathcal{N}} - B^{2\mathcal{N}}\,(R^{2s})^{-1}\,(B^{2\mathcal{N}})^T\Pi^{2\mathcal{N}}\right] z^{2\mathcal{N}}(t) \\ &- \ B^{2\mathcal{N}}\,(R^{2s})^{-1}\,(B^{2\mathcal{N}})^T r^{2\mathcal{N}}(t) + G^{2\mathcal{N}}(t) \\ z^{2\mathcal{N}}(0) &= 0 \ . \end{aligned} \tag{18}$$

The Riccati variable $\Pi^{2\mathcal{N}}$ and tracking variable $r^{2\mathcal{N}}(t)$ satisfy the equations

$$(A^{2\mathcal{N}})^T\Pi^{2\mathcal{N}} + \Pi^{2\mathcal{N}}A^{2\mathcal{N}} - \Pi^{2\mathcal{N}}B^{2\mathcal{N}}\left(R^{2s}\right)^{-1}(B^{2\mathcal{N}})^T\Pi^{2\mathcal{N}} + Q^{2\mathcal{N}} = 0 \ , \tag{19}$$

and

$$\begin{aligned} \dot{r}^{2\mathcal{N}}(t) &= -[A^{2\mathcal{N}} - B^{2\mathcal{N}}\,(R^{2s})^{-1}\,(B^{2\mathcal{N}})^T\Pi^{2\mathcal{N}}]^T r^{2\mathcal{N}}(t) + \Pi^{2\mathcal{N}}G^{2\mathcal{N}}(t) \\ r^{2\mathcal{N}}(\tau) &= 0 \ , \end{aligned} \tag{20}$$

respectively.

In the following simulations, twelve patch pairs bonded to the shell were used as actuators. The dimensions and material properties for both the shell and patches are given in Table 1. All patches were assumed to have a uniform dimension of x length $= 0.1m$ and θ width $= \pi/6$ with the location of the center of each pair summarized in Table 1. The matrix $Q^{2\mathcal{N}}$ was taken to be

$$Q^{2\mathcal{N}} = \begin{bmatrix} d_1 I & & & \\ & d_2 I & & \\ & & \ddots & \\ & & & d_6 I \end{bmatrix}_{2\mathcal{N}\times 2\mathcal{N}} \times \begin{bmatrix} K_E^{\mathcal{N}} & \\ & M^{\mathcal{N}} \end{bmatrix}_{2\mathcal{N}\times 2\mathcal{N}} \ , \tag{21}$$

where I is the identity matrix, $M^{\mathcal{N}}$ is the mass matrix and $K_E^{\mathcal{N}}$ denotes the stiffness matrix. The matrix of control weights R^{2s} was taken to be the diagonal matrix $R^{2s} = r \cdot I^{2s \times 2s}$. The parameters $d_i, i = 1, \ldots, 6$ and r were used to maximize attenuation and limit voltage input to the patches to approximately 100 volts rms. In the simulations reported on here, we used $d_i = 10^{13}, i = 1, \ldots, 6$, and $r = 50$. Time histories are again recorded at the point p_1. To further demonstrate the controlled system, root mean square displacements at the lines L_1 and L_2 are plotted (see Figure 2 for the location of p_1, L_1 and L_2 on the shell). At each point on the RMS lines, 500 displacements were recorded and the root mean square displacements on L_1 in the longitudinal direction were computed using the relation

$$L_1^{RMS}(x) = \sqrt{\frac{1}{500} \sum_{i=0}^{500} u^{\mathcal{N}}(t_i, x, \pi/6)^2} \ , \ 0 \leq x \leq \ell \ .$$

RMS displacements in the other directions and on L_2 are calculated similarly.

In Figure 4, we present full order, uncontrolled and controlled RMS displacements together with controlled RMS displacements for the Lagrange ($\mathcal{N} = 9$) and POD ($\mathcal{N} = 9$) reduced order models. Time histories at the point p_1 in the full order, Lagrange and POD reduced order models are depicted in Figure 5. We point out that great difficulty was encountered in obtaining full order Riccati solutions due to large matrix dimensions and ill conditioning. Better attenuation is attained with reduced order models (than with full order models) due to smaller matrix dimensions resulting in better conditioning of the mass and stiffness matrices and hence more accurate Riccati solutions.

Displacement and RMS plots with $\mathcal{N} = 6$ and 12 for both Lagrange and POD reduced order models are similar to those reported in Figures 4 and 5. Although good attenuation was obtained for Lagrange and POD reduced order models using $\mathcal{N} = 3$ basis functions, the full order system was not fully resolved by the reduced order model so results are not presented here.

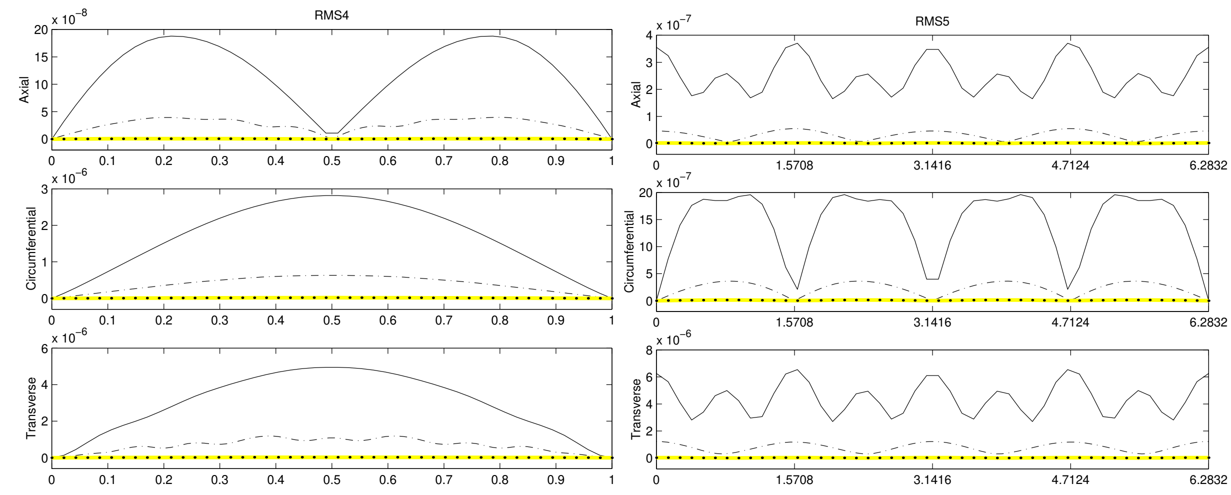

(a) (b)

Figure 4. Uncontrolled and controlled RMS displacements; —— full order uncontrolled ($\mathcal{N}$ = 333), – · – full order controlled ($\mathcal{N} = 333$), —— Lagrange controlled ($\mathcal{N} = 9$), $\cdots$ POD controlled ($\mathcal{N} = 9$); (a) axial line L_1; (b) circumferential line L_2.

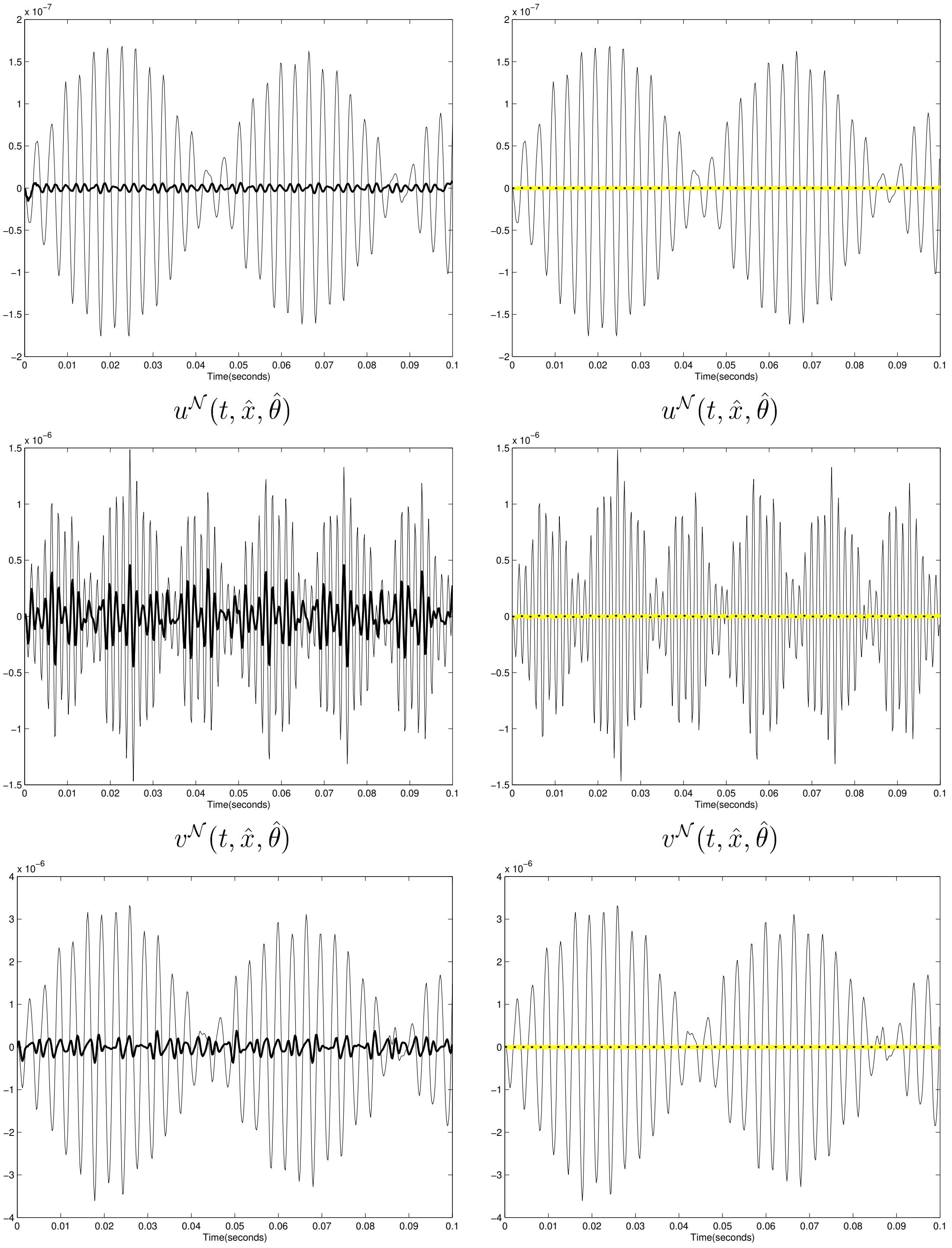

$u^{\mathcal{N}}(t,\hat{x},\hat{\theta})$ $u^{\mathcal{N}}(t,\hat{x},\hat{\theta})$

$v^{\mathcal{N}}(t,\hat{x},\hat{\theta})$ $v^{\mathcal{N}}(t,\hat{x},\hat{\theta})$

$w^{\mathcal{N}}(t,\hat{x},\hat{\theta})$ $w^{\mathcal{N}}(t,\hat{x},\hat{\theta})$

(a) (b)

Figure 5. Uncontrolled and controlled displacements at p_1; (a) full order ($\mathcal{N} = 333$): —— uncontrolled, ━━ controlled; (b) reduced order: —— uncontrolled, —— Lagrange controlled ($\mathcal{N} = 9$), $\cdots$ POD controlled ($\mathcal{N} = 9$).

Reduced order gains applied to the full order system

One primary goal of this research is to develop a method to compute control gains from observations of a physical shell system using a discretized PDE model and implement the computed control gains in real time to the physical system. Numerical results from model reduction techniques given in previous sections indicate the feasibility of real time computation by reducing the number of unknowns without degrading the performance of the model and without losing control authority. While studies of the reduced order controllers applied to the reduced order model dynamics are useful, they do not truly indicate the performance of the controller when applied in practice. To obtain information in this regard, we next investigated the performance of control gains computed from the reduced order model when applied to the full order system. It has been shown through careful analysis of natural frequencies and modes in [7] that the full order system closely approximates the infinite dimensional system. With this assumption, applying the reduced order gains to the full order system is a reasonable way to investigate the anticipated performance of the method when used on an actual physical system. While our early calculations give *some* indication of how a feedback gain based on reduced order models might perform when applied to either the true infinite dimensional system or even a large finite dimensional model, the results are only suggestive. Further evidence will be available once reduced order model based controllers are implemented experimentally.

We illustrate the use of POD reduced order gains in controlling the full order system, but the method we present could be readily adapted for the Lagrange, Hermite or Taylor reduced basis methods.

We denote the full order space by $V^{\mathcal{N}}$ and the POD reduced basis space by $V^{\mathcal{N}_P}$. To employ a POD reduced order based optimal control in the full order equation

$$\dot{z}^{2\mathcal{N}}(t) \quad = \quad A^{2\mathcal{N}} z^{2\mathcal{N}}(t) + B^{2\mathcal{N}} U(t) + G^{2\mathcal{N}}(t) \; , \tag{22}$$

we must find a projection $\hat{P} : \mathbb{R}^{2\mathcal{N}} \to \mathbb{R}^{2\mathcal{N}_P}$ so that we can employ the reduced order feedback gains with full order observations in

$$U(t) = -\left(R^{2s}\right)^{-1} \left(B^{2\mathcal{N}_P}\right)^T \left[\Pi^{2\mathcal{N}_P} \hat{P} z^{2\mathcal{N}}(t) - r^{2\mathcal{N}_P}(t)\right] \; . \tag{23}$$

To this end, note first that the Galerkin approximation $y^{\mathcal{N}}$ (of the solution to (5)) is the projection of the infinite dimensional solution y into the finite dimensional subspace $V^{\mathcal{N}}$. Similarly, it follows that $y^{\mathcal{N}_P}$ is the projection of y into $V^{\mathcal{N}_P}$. Denote the projection operator from V into $V^{\mathcal{N}_P}$ by $\mathcal{P}^{\mathcal{N}_P}$ and denote the projection from $V^{\mathcal{N}}$ into $V^{\mathcal{N}_P}$ by $\mathcal{P}^{\mathcal{N}_P}_{V^{\mathcal{N}}}$. Since the same inner products are used in $V, V^{\mathcal{N}}$ and $V^{\mathcal{N}_P}$ and $V^{\mathcal{N}_P} \subset V^{\mathcal{N}} \subset V$, it follows that

$$\mathcal{P}^{\mathcal{N}_P} y^{\mathcal{N}} = \mathcal{P}^{\mathcal{N}_P}_{V^{\mathcal{N}}} y^{\mathcal{N}} = y^{\mathcal{N}_P} \quad \text{for all } y^{\mathcal{N}} \in V^{\mathcal{N}} \; .$$

This implies that the reduced order state $(y^{\mathcal{N}_P}, \dot{y}^{\mathcal{N}_P}) \in V^{\mathcal{N}_P} \times V^{\mathcal{N}_P}$ is the projection of the full order state $(y^{\mathcal{N}}, \dot{y}^{\mathcal{N}}) \in V^{\mathcal{N}} \times V^{\mathcal{N}}$ from $V^{\mathcal{N}} \times V^{\mathcal{N}}$ into $V^{\mathcal{N}_P} \times V^{\mathcal{N}_P}$, which is equivalent to mapping the vector of basis coefficients $z^{2\mathcal{N}}$ into $z^{2\mathcal{N}_P}$ (the vector $z^{2\mathcal{N}}$ is defined following (10)). We obtain this projection by pre-multiplying $z^{2\mathcal{N}}$ by the matrix representation of the projection $\mathcal{P}^{\mathcal{N}_P}_{V^\mathcal{N}} \times \mathcal{P}^{\mathcal{N}_P}_{V^\mathcal{N}}$ from $V^\mathcal{N} \times V^\mathcal{N}$ into $V^{\mathcal{N}_P} \times V^{\mathcal{N}_P}$. Denoting the matrix representation of $\mathcal{P}^{\mathcal{N}_P}_{V^\mathcal{N}}$ by $\bar{P}^{\mathcal{N}_P}$, then $\hat{P}$ which we use in (23) is then given by

$$\hat{P} = \begin{bmatrix} \bar{P}^{\mathcal{N}_P} & \\ & \bar{P}^{\mathcal{N}_P} \end{bmatrix} . \tag{24}$$

Note that $\hat{P}$ is the matrix representation of $\mathcal{P}^{\mathcal{N}_P}_{V^\mathcal{N}} \times \mathcal{P}^{\mathcal{N}_P}_{V^\mathcal{N}}$. The reduced order gains applied in the full order feedback loop, i.e., (23) employed in (22), yields the full order closed loop

$$\begin{aligned} \dot{z}^{2\mathcal{N}}(t) &= \left[A^{2\mathcal{N}} - B^{2\mathcal{N}} R^{-1} \left(B^{2\mathcal{N}_P}\right)^T \Pi^{2\mathcal{N}_P} \hat{P}\right] z^{2\mathcal{N}}(t) \\ &\quad + B^{2\mathcal{N}} R^{-1} \left(B^{2\mathcal{N}_P}\right)^T r^{2\mathcal{N}_P}(t) + G^{2\mathcal{N}}(t) \; . \end{aligned} \tag{25}$$

The computation and structure of the matrix $\bar{P}^{\mathcal{N}_P} \in \mathbb{R}^{\mathcal{N}_P \times \mathcal{N}}$ is dictated by the component nature of the state $y = (u, v, w)$. The spaces $V^\mathcal{N}$ and $V^{\mathcal{N}_P}$ are product spaces as expressed in (7), so the projection $\mathcal{P}^{\mathcal{N}_P}_{V^\mathcal{N}}$ has three components

$$\begin{aligned} \mathcal{P}^{N^u_P} &: \; \text{span}\,\{\mathcal{B}_{u_i}\}_{i=1}^{\mathcal{N}_u} \to \text{span}\,\{\Phi_{u_i}\}_{i=1}^{N_P} \\ \mathcal{P}^{N^v_P} &: \; \text{span}\,\{\mathcal{B}_{v_i}\}_{i=1}^{\mathcal{N}_v} \to \text{span}\,\{\Phi_{v_i}\}_{i=1}^{N_P} \\ \mathcal{P}^{N^w_P} &: \; \text{span}\,\{\mathcal{B}_{w_i}\}_{i=1}^{\mathcal{N}_w} \to \text{span}\,\{\Phi_{w_i}\}_{i=1}^{N_P} \; , \end{aligned}$$

where N_p is the number of POD basis functions in the u, v and w directions with basis functions Φ_{u_i}, Φ_{v_i} and Φ_{w_i}, and $\mathcal{N}_u, \mathcal{N}_v$ and $\mathcal{N}_w$ denote full order discretization levels with basis functions $\mathcal{B}_{u_i}, \mathcal{B}_{v_i}$ and $\mathcal{B}_{w_i}$. Denoting the matrix representation of the component projections by $\bar{P}^{N^u_P}$, $\bar{P}^{N^v_P}$ and $\bar{P}^{N^w_P}$, the matrix $\bar{P}^{\mathcal{N}_P}$ has the components

$$\bar{P}^{\mathcal{N}_P} = \begin{bmatrix} \bar{P}^{N^u_P} & & \\ & \bar{P}^{N^v_P} & \\ & & \bar{P}^{N^w_P} \end{bmatrix} .$$

We illustrate the construction of $\bar{P}^{N^u_P}$ and point out that the construction of $\bar{P}^{N^v_P}$ and $\bar{P}^{N^w_P}$ are carried out similarly. For $i = 1, \ldots, N_P$ and any $u^\mathcal{N} \in \text{span}\,\{\mathcal{B}_{u_i}\}_{i=1}^{\mathcal{N}_u}$, the projection $\mathcal{P}^{N^u_P}$ satisfies $\left\langle \mathcal{P}^{N^u_P} u^\mathcal{N} - u^\mathcal{N}, \Phi_{u_i} \right\rangle = 0$. It follows that $\left\langle \mathcal{P}^{N^u_P} u^\mathcal{N} - \sum_{j=1}^{\mathcal{N}_u} u_j \mathcal{B}_{u_j}, \Phi_{u_i} \right\rangle = 0$ and hence

$$\left\langle \sum_{k=1}^{N_P} (\bar{P}^{N^u_P} \bar{u})_k \Phi_{u_k} - \sum_{j=1}^{\mathcal{N}_u} u_j \mathcal{B}_{u_j}, \Phi_{u_i} \right\rangle = 0 \; , \quad i = 1, \ldots, N_P \; ,$$

where $\bar{u}$ is the vector of coefficients $u_1, \ldots, u_{\mathcal{N}_u}$ in the full order space. The equality $\mathcal{P}^{N^u_P} u^\mathcal{N} = \sum_{k=1}^{N_P} (\bar{P}^{N^u_P} \bar{u})_k \Phi_{u_k}$ used above expresses the property of matrix representations where the basis coefficients of the image (i.e., the basis coefficients of $\mathcal{P}^{N^u_P} u^\mathcal{N}$ in $\text{span}\,\{\Phi_{u_i}\}_{i=1}^{N_P}$) are obtained by multiplying the matrix representation and the vector of basis coefficients in the domain (i.e., $\bar{P}^{N_P^u}\bar{u}$). We use the linearity properties of the inner product to obtain

$$\sum_{k=1}^{N_P}(\bar{P}^{N_P^u}\bar{u})_k \langle \Phi_{u_k}, \Phi_{u_i}\rangle = \sum_{j=1}^{\mathcal{N}_u} u_j \left\langle \mathcal{B}_{u_j}, \Phi_{u_i}\right\rangle , \quad i = 1, \ldots, N_P \ .$$

Since this equation is true for $i = 1, \ldots, N_P$, we then form a matrix equation

$$M_1^{N_P\times N_P}(\bar{P}^{N_P^u}\bar{u}) = M_2^{N_P\times\mathcal{N}_u}\bar{u} \ ,$$

where $M_1 \in \mathbb{R}^{N_P\times N_P}$ has components

$$[M_1]_{k,\ell} = \langle \Phi_{u_\ell}, \Phi_{u_k}\rangle \ , \ k, \ell = 1, \ldots, N_P \ ,$$

and $M_2 \in \mathbb{R}^{N_P\times\mathcal{N}_u}$ has components

$$[M_2]_{k,\ell} = \langle \mathcal{B}_{u_\ell}, \Phi_{u_k}\rangle \ , \ \ell = 1, \ldots, N_P, \ k = 1, \ldots, \mathcal{N}_u \ .$$

Therefore $\bar{P}^{N_P{}^u} = M_1^{-1}M_2 \in \mathbb{R}^{N_P\times\mathcal{N}_u}$. The other two matrix representations $\bar{P}^{N_P{}^v}$ and $\bar{P}^{N_P{}^w}$ are created similarly. Once these matrices are computed, the matrix $\hat{P} \in \mathbb{R}^{2\mathcal{N}_P\times 2\mathcal{N}}$ is formed and we obtain the full order feedback loop based on reduced order control gains in (25).

In Figures 6 and 7, we present time history and RMS plots when the feedback control based on $\mathcal{N} = 9$ POD basis functions is implemented in the full order system. As might be expected, the resulting attenuation is not as good as when the reduced order control is applied in the reduced order model. However, the overall effectiveness of the feedback control is still quite impressive. Results with $\mathcal{N} = 6$ POD basis functions are similar. Since the system was not resolved with $\mathcal{N} = 3$ POD basis functions (as indicated in Table 3), good attenuation was not obtained (see [3, p. 31]) in the case $\mathcal{N} = 3$.

Somewhat surprisingly, good attenuation using $\mathcal{N} = 12$ POD basis functions *was not* attained. Indeed, computations suggested great difficulty in stabilizing the system based on 12 POD element designs. An analysis of the controllability matrix of the POD reduced order system suggests a possible explanation. Its rank continues to decrease (as more POD elements are used) relative to the maximum possible rank until the system becomes significantly uncontrollable (see [3, Table 9] for the ranks of the controllability matrices with $\mathcal{N} = 3, 6, 9$ and 12 POD basis functions). Therefore, as we increase the number of POD basis functions, the system becomes increasingly more difficult to stabilize. Since stabilizing feedback control in the reduced order model is already more difficult with 12 basis functions than with 9, then stabilizing control in the full order model is likely to be much more difficult.

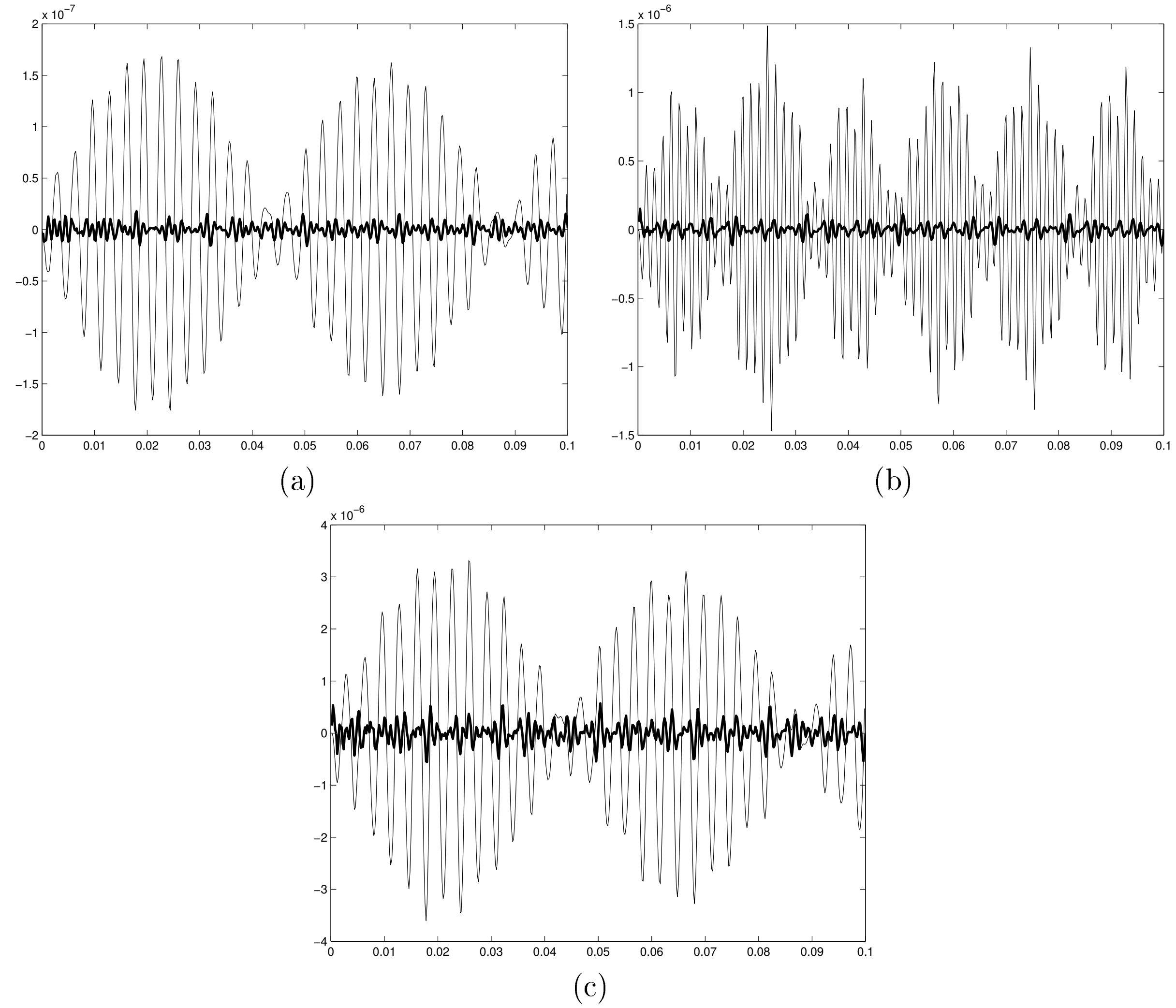

Figure 6. Full order uncontrolled and controlled displacements at p_1 with control design based on $\mathcal{N} = 9$ POD basis functions; (a) longitudinal $u^{\mathcal{N}}(t, \hat{x}, \hat{\theta})$, (b) circumferential $v^{\mathcal{N}}(t, \hat{x}, \hat{\theta})$, (c) transverse $w^{\mathcal{N}}(t, \hat{x}, \hat{\theta})$; —— (uncontrolled), **——** (controlled).

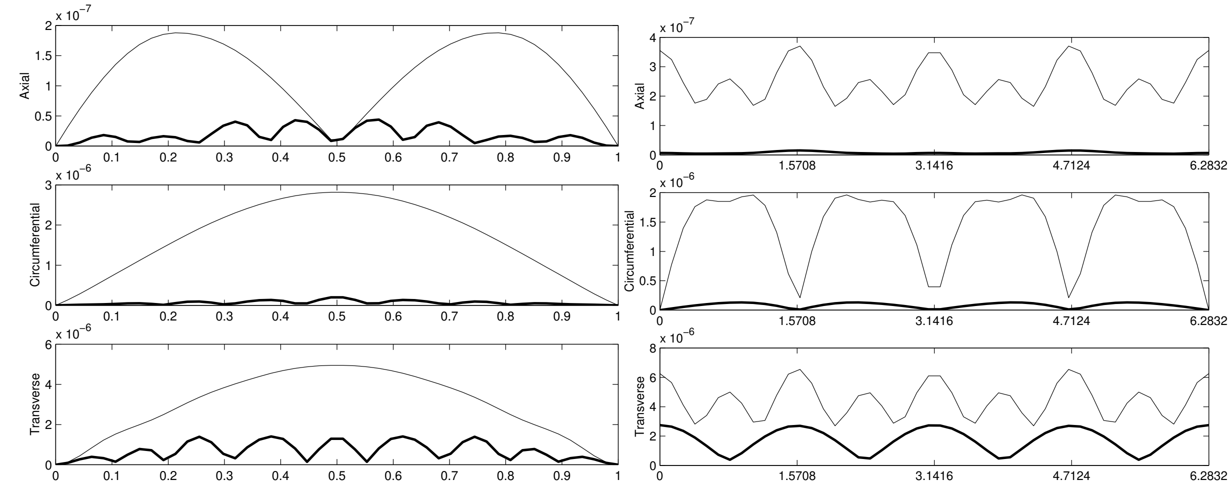

(a) (b)

Figure 7. Full order uncontrolled and controlled root mean square displacements with control design based on $\mathcal{N} = 9$ POD basis functions; (a) axial line L_1, (b) circumferential line L_2; —— (uncontrolled), **——** (controlled).

5 Concluding Remarks

These preliminary computational investigations on the use of reduced order model based feedback control design suggest several positive features of such an approach. When they are effective, these designs can offer significant control authority with substantially reduced on-line computational requirements. Very low order designs (with cheap calculations) sufficed in several of the examples we tested. Both Lagrange and POD based reduced basis methods can be effective, but both also have the potential for significant difficulties. By their very nature, controllability deficiencies are inherent in both approaches and can in some cases render the methods useless. Increasing the order of approximation in the system can yield a badly uncontrollable system for which the design is destabilizing.

The Lagrange reduced basis methods offer no systematic way to increase the level of approximation, and ill-conditioning of system matrices can thwart efforts at increased accuracy in approximations. For the POD based methods, there is a systematic, optimal way to improve the level of approximation. Moreover, one can retain well-conditioned system matrices in doing this. In theory and in "textbook" examples (applying POD designed controllers to the POD system itself), the methods work well with increased order of approximation leading to improved results. However, in practice (use of POD based control designs in the full order model) controllability and stabilizability features (deficits) can become worse as one increases the number of basis elements.

Our preliminary calculations suggest that reduced order model feedback control design ideas are worth pursuing. While they may prove quite adequate in some applications, there is still much to be learned. Our extensions of these ideas to compensator design and application to nonlinear system dynamics is currently underway but is in its infancy. We are also in the process of developing laboratory experiments to test the practical feasibility of the methods. It is somewhat early to make a definitive statement about the effectiveness of reduced order model design in general and POD design in particular in feedback control applications, especially for nonlinear systems.

References

[1] B.O. Almroth, "Automatic choice of global shape functions in structural analysis," *AIAA Journal*, 16 (1978), pp. 525-528.

[2] H.T. Banks, M. Demetriou and R.C. Smith, "Utilization of coupling effects in compensator design for structural acoustic systems – numerical examples," *Journal of the Acoustical Society of America*, 103 (1998), pp. 872-887.

[3] H.T. Banks, R.C.H. del Rosario and R.C. Smith, "Reduced Order Model Feedback Control Design: Computational Studies for Thin Cylindrical Shells," Tech. Rep. CRSC-TR98-25, Center for Research in Scientific Computation, NC State University, June, 1998.

[4] H.T. Banks, R.C Smith, D. Brown, R. Silcox and V. Metcalf, "Experimental confirmation of a PDE-based approach to design of feedback controls," *SIAM Journal on Control and Optimization*, 35 (1997), pp. 1263-1296.

[5] H.T. Banks, R.C. Smith and Y. Wang, *Smart Material Structures: Modeling, Estimation and Control*, Masson/John Wiley, Paris/Chichester, 1996.

[6] G. Berkooz, P. Holmes, and J.L. Lumley, "The proper orthogonal decomposition in the analysis of turbulent flows," *Annual Review of Fluid Mechanics*, 25 (1993), pp. 539-575.

[7] R. del Rosario and R.C. Smith, "Spline approximation of thin shell dynamics," *International Journal for Numerical Methods in Engineering*, 40 (1997), pp. 2807-2840.

[8] R. del Rosario and R.C. Smith, "LQR control of shell vibrations via piezoceramic actuators," *International Series in Numerical Mathematics* (F. Kappel and K. Kunisch, eds.) Birkhäuser, Basel, 126 (1998), pp. 247-264.

[9] R. del Rosario and R.C. Smith, "LQR control of thin shell dynamics: formulation and numerical implementation," ICASE Report 97-59, NASA Langley Research Center, November, 1997; *Journal of Intelligent Material Systems and Structures*, to appear.

[10] K. Ito and S.S. Ravindran, "A reduced order method for simulation and control of fluid flows," Tech. Rep. CRSC-TR96-27, Center for Research in Scientific Computation, NC State University, September, 1996; *Journal of Computational Physics*, submitted.

[11] K. Ito and S.S. Ravindran, "A reduced basis method for control problems governed by PDE," Tech. Rep. CRSC-TR97-1, Center for Research in Scientific Computation, NC State University, January, 1997; *International Series in Numerical Mathematics*, (F. Kappel and K. Kunisch, eds.), Birkhäuser, Basel, 126 (1997).

[12] A.W. Leissa, *Vibration of Shells,* NASA SP-288, 1973; reprinted by the Acoustical Society of America through the American Institute of Physics, 1993.

[13] J.L. Lumley, "The structure of inhomogenous turbulent flows," *Atmospheric Turbulence and Wave Propagation* (A.M. Yaglom and V.I. Tatarski, eds.), Nanka, Moscow, 1967, pp. 166-178.

[14] H.V. Ly and H.T. Tran, "Proper orthogonal decomposition for flow calculations and optimal control in a horizontal CVD reactor," Tech. Rep. CRSC-TR98-13, Center for Research in Scientific Computation, NC State University, March, 1998; *Quarterly of Applied Mathematics*, to appear.

[15] D.A. Nagy, "Modal representation of geometrically nonlinear behavior by the finite element method," *Computers and Structures*, 10 (1979), pp. 683-688.

[16] A.K. Noor and J.M. Peters, "Reduced basis technique for nonlinear analysis of structures," *AIAA Journal*, 18 (1980), pp. 455-462.

[17] A.K. Noor, C.M. Andersen and J.M. Peters, "Reduced basis technique for collapse analysis of shells," *AIAA Journal*, 19 (1981), pp. 393-397.

[18] A.K. Noor, "Recent advances in reduction methods for nonlinear problems," *Computers and Structures*, 13 (1981), pp. 31-44.

[19] J.S. Peterson, "The reduced basis method for incompressible viscous flow calculations," *SIAM Journal on Scientific and Statistical Computing*, 10 (1989), pp. 777-786.